CHARACTERISTICS OF A COMPLIANT FLUID-MECHANICAL ACTUATOR FOR CREATING A SCREW MOTION - COMPARISON OF SIMULATION AND MEASUREMENT RESULTS

Griebel, Stefan*; Feierabend, Martin *; Bojtos, Attila**; Zentner, Lena*

* Technische Universität Ilmenau, Mechanism Technology Group
** Budapest University of Technology and Economics, Department of Mechatronics, Optics and Engineering Informatics

ABSTRACT

In this paper a compliant fluid-mechanical actuator which provides a screw motion for adduction of dry electrodes on the surface of the head is investigated. The simulated and measured characteristics with and without a load torque are compared. The compliant fluid-mechanical actuator is one piece, hollow on the inside and consists of a helical twisted lateral area. Its height and diameter are 50 mm. It consists of silicone Elastosil® M 4644 and can be used in a pressure range from 0 to 1 bar. Advantageously, the actuator reaches a rotational angle of approximately 100° and a stroke of about 29 mm. These values can be increased by load torque. In the pressure range of $0 \leq p \leq 500$ mbar, the actuator operates mainly on the principle of folding. In addition, it generates a nearly linear screw curve. In the pressure range of $500 < p \leq 1000$ mbar, it operates mainly on the principle of strain. Hence, the actuator generates a stroke that is almost independent of the load torque. Furthermore, the deviations of rotation angle and stroke of the Ansys® FEM simulation model and of the functional model are in the pressure range of $p \geq 200$ mbar without load torque, in consideration of an experimentally determined friction torque that is less than 10 %. The simulation models can be used in addition to the development and investigation of fluid-mechanical actuators.

Index Terms – fluid-mechanical actuator, compliant, screw motion, silicone elastomer, and finite element analysis

1. INTRODUCTION

If neural brain activity needs to be assessed, the bioelectric potential fluctuations in the head are measured with an electroencephalogram (EEG). In clinical daily routine, silver/silver chloride (Ag/AgCl) electrodes are used. During the time-consuming preparation procedure, electrically conductive gels or pastes are placed between each electrode and the scalp. Thereby, the transition impedances are reduced so that the recording of the bioelectric potential is possible. The use of conductive pastes respectively gels can cause skin irritation and have a limited shelf-life during long-term measurements. Hence, this research focuses on the use of dry electrodes [1-4]. These can be applied without gels or pastes; however, they need a stable and reproducible introduction to the head surface. For these requirements, fluid-mechanical actuators made of biomedical silicone have high potential [5-8]. These enable a change in their geometric shape by changing their internal fluid pressure. Hence, they can transfer purposeful motion variables, like stroke and angle, as well as forces and, depending on the geometric shape, also torques. Fig. 1 shows a classification of possible deformation principles of fluid-mechanical actuators. Advantageous principles of deformation within an application in the biomedical sector are folding and rolling up. Here, the strain occurring in

the material is less during deformation by stretching. Furthermore, a higher number of operating cycles is possible with lower failure probability [9].

```
              ┌─────────────────────────┐
              │ Principle of deformation │
              └─────────────────────────┘
         ┌──────────────┼──────────────┐
         ▼              ▼              ▼
   ┌────────────┐  ┌──────────┐  ┌────────────┐
   │ Stretching │  │ Folding  │  │ Rolling up │
   └────────────┘  └──────────┘  └────────────┘
    e.g.: [10]      e.g.: [5]      e.g.: [11]
```
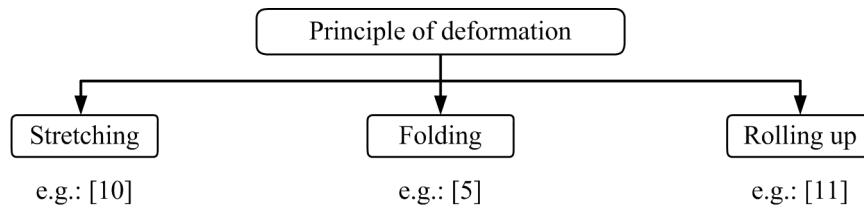
Fig. 1. Possible deformation principles of fluid-mechanical actuators with examples

If these fluid actuators are mounted in an EEG cap, then it is possible to generate a force by increasing the internal pressure of the actuator. Accordingly, the existing contact pressure increases between the electrode and the scalp. In this way, the contact resistance between each dry electrode and the head is reduced, to the extent that an EEG measurement is possible [12]. If additionally a rotation and a torque are generated, then a relative motion can be produced between the head skin and the electrode. These relative motions are helpful for penetrating the hair layer.

If a number ≥ 128 dry electrodes are distributed on the head, the diameter of the fluid-mechanical actuator must be less than 16 mm [13]. The motion variables, stroke and angle of rotation, of such small structures can be determined and compared by means of simulation and an experimental setup [13]. However, the experimental determination of the force generated in the stroke direction and the torque in the rotational direction with the assembly presented in [13] is not possible. For this reason, a further experimental setup was designed, for measuring the motion variables and the producible torque under the influence of load torque and counterforce while increasing fluid pressure. For easy measurement, a manageable fluid-mechanical actuator has been developed, which has a height and diameter of 50 mm.

The aim of the paper is to detect a small difference less than 10 % between the simulation model and functional model. In addition to this, simulation models can be used for future developments of fluid-mechanical actuators.

2. DESIGN OF THE FLUID-MECHANICAL ACTUATOR

The fluid-mechanical actuator is required to produce a screw motion with a rotation of at least 90° and with a stroke of at least 50% of the height of the fluid-mechanical actuator. The dimensions of the fluid actuator without clamping surfaces should not exceed a volume cube of 50 mm edge length. The operating pressure should not exceed 1 bar. In addition, the geometric shape should be simple, and thus have a minimal number of geometrical parameters in order to enable simple production later. Furthermore, the fluid-mechanical actuator should be a single piece.

Various basic solutions in principle were designed and evaluated using different heavily weighted evaluation criteria to select an approach for the implementation [14].

The developed compliant fluid-mechanical actuator is a one-piece, hollow on the inside and consists of a helical twisted lateral area with a height $h_F = 50$ mm and a diameter $h_F = 50$ mm (see sectional view of Fig. 2). One side is monolithic and closed with a cylindrical body (connector) with a height $h_z = 2$ mm and a diameter $d_z = 60$ mm ($R_Z = 30$ mm). The second side, which serves for supplying compressed air, is also monolithically connected to a cylindrical connector, but is pierced by the hollow spirally wound element (cavity) (see. top view, side view and bottom view in Fig. 2).
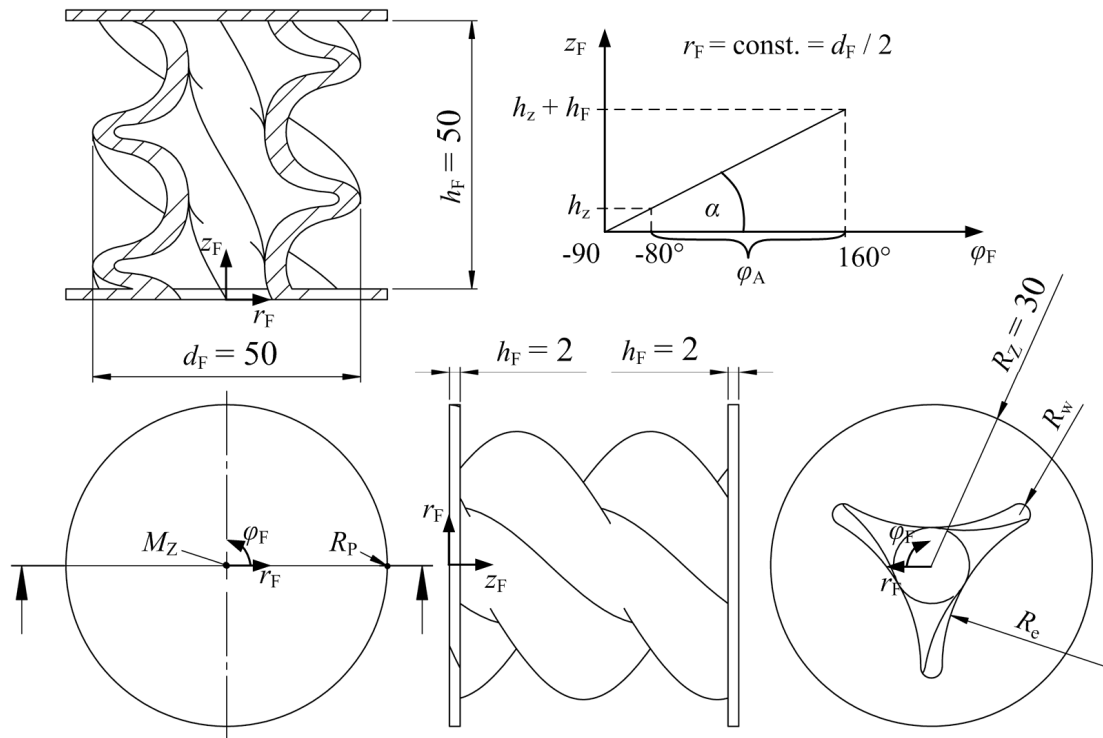
Fig. 2. Final compliant fluid-mechanical actuator; above f. l. t. r.: sectional view and helix from point (d_F / 2, -90°, 0) to point (d_F / 2, 160°, $h_z + h_F$) at the cylindrical coordinate system; bottom f. l. t. r.: top view, lateral view and bottom view at the cylindrical coordinate system

The geometry of the cavity is formed by extrusion of the cross-section along a spiral parallel to the inertial section. The spiral represented in the cylindrical coordinate system in Fig. 2 begins at a boundary point of the cross-section area and is perpendicular to the latter. The helix angle α and the extrusion path are defined by an initial rotation φ_A of the fluid actuator of 240° in the direction of φ_F. The cross-section area consists of $n = 3$ semicircular convex curves of the same radius $R_w = 2$ mm, which are distributed uniformly on the circumference. The convex curves are connected by tangential subsequent concave curves of the radius R_e. Furthermore, the spirally wound fluid actuator has a uniform thickness of $d = 4$ mm to meet the operating pressure requirement of 1000 mbar.

3. MATERIAL AND METHODS

3.1 Production of a Functional Model

Because of the large number of undercuts, injection molding was chosen as the method for producing the functional model. Also, a mold was designed. The insertion of the molding tool which forms the interior and exterior surfaces was prepared by means of rapid prototyping in the fused deposition method (Dimension Elite, alphacam GmbH, Schorndorf, Germany). The inner surface of the fluid actuator was formed by means of one insertion, and the outside of the lateral surface by means of four insertions. These five insertions were positioned with each other in a half mold made of aluminum, which was screwed together with a second half mold. Hence, the position of the components could be fixed to each other. In one of the two mold halves was a reservoir in which the 2-component silicone (Elastosil® M 4644, Wacker Chemie AG, Munich, Germany), de-aerated by vacuum, was filled. The silicone was injected

into the mold using a piston. After a waiting time of 24 hours at room temperature, the actuator was demolded.

3.2 Measurement at the Functional Model

A measurement setup was designed and built to investigate the functional model (see Fig. 3). The compliant fluid-mechanical actuator (9) was attached air-tightly with two mounting plates (8) and (10) on each of its two circular end faces. On the left side of the actuator in Fig. 3, the rotation about the z-axis was allowed, while on the right side of the actuator the displacement was in the z-direction. The allowed rotation drives an axle shaft, which is mounted via a fixed bearing (7) and a movable bearing (6). At one end of this axle shaft a torque measuring shaft (4) (DATAFLEX® 16/10 KTR GmbH, Rheine, Germany) is connected via a torsionally stiff self-aligning coupling (5) (Radex® - NC 15 KTR GmbH, Rheine, Germany) with zero clearance. At the other end, an identical coupling (3) is connected to a further axle shaft. This axle shaft is mounted by means of a loose bearing (2). At the end of the shaft, a circular disk (1) is fixed, to which different masses m can be attached by a cable. Hence, a constant load torque M_L can be generated (neglecting the changing rope length and thus rope mass). Thus, a negative load torque increases the initial rotation φ_A and the actuator decreases its length at the same time. A positive load torque decreases the initial rotation φ_A and the actuator increases its length.
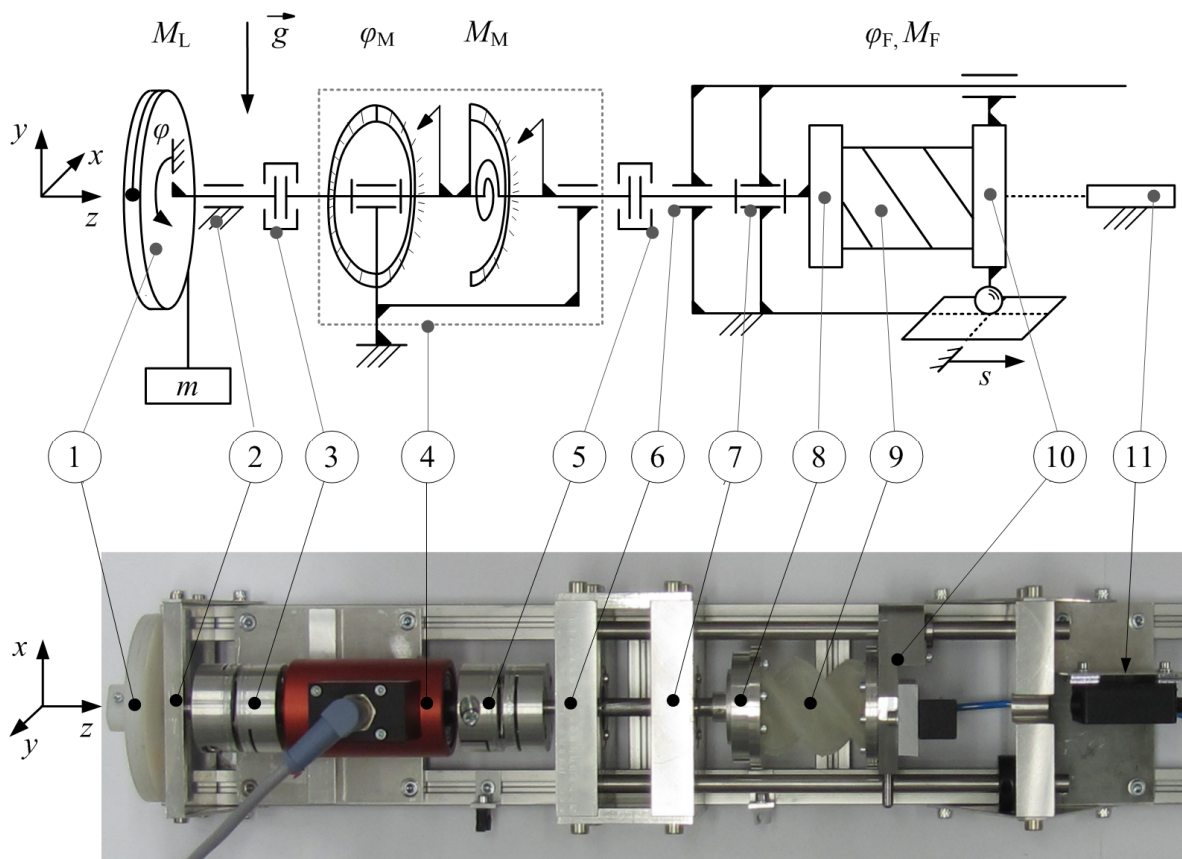

Fig. 3. Principle sketch and measurement setup built for determining the output variables of the compliant fluid-mechanical actuator

The right side of the actuator is guided eccentrically by a guideway with a degree of freedom f of two and a further component part mating with a degree of freedom of five. The fluid actuator (9) is supplied with compressed air by the aluminum component part (10). The inner

pressure p of the fluid actuator is recorded (analog) by means of a pressure gauge (DMU4 0-1999 mbar, Kalinsky Sensor Electronics GmbH & Co. KG, Erfurt, Germany). In addition the pressure is controlled by a proportional pressure control valve (VPPM-6L-L-G18-0L-2h-V1N-S1, Festo AG & Co.KG, St. Ingbert-Rohrbach, Germany). The displacement in the z-direction represented by the coordinate s is measured with a laser displacement sensor (11) (LD optoNCDT 1605-20, Micro-Epsilon Messtechnik, Ortenburg, Germany) using the triangulation method with a measurement accuracy of 1 micron. By means of the torque measuring shaft, the rotation of the axle shaft φ_M can be measured with a measuring accuracy of $\pm 0.25°$ and the torque M_M can be measured with a measurement accuracy of < 0.01 Nm. All signals were digitized using a 16-bit multifunction data acquisition card (NI PCI-6221, National Instruments Germany GmbH, Munich, Germany). The functional model of the fluid actuator was loaded for different load torques M_L from -0.4 to +0.2 Nm in steps of 0.2 Nm with a maximum pressure p from 0 to 1000 mbar in steps of 50 mbar. The pressure p was discretely adjusted by the operator with a LabVIEW® program which controls the pressure control valve. After reaching the desired value of the pressure, the applied pressure p, the torque M_M, the rotation φ_M and the hub s were recorded by the same LabVIEW® program.

3.3 Simulation of the Compliant Fluid-mechanical Actuator

For the simulation, a parametric model was designed in SolidWorks 2012, which was read into Ansys® 14.5. It was chosen to use the nonlinear material law, Ogden 2nd order, for modeling the silicone material with shore hardness A of 40. This material law is based on experimental data from a uniaxial tensile test and a pure shear test each up to 100% nominal engineering strain [13]. The material constants are listed in Table 1.

Tab. 1. Material constants determined for the constitutive law, Ogden 2nd order, for simulation of the used silicone Elastosil® 4644

Material constant	μ_1	α_1	μ_2	α_2
Value	0.00176 MPa	11.915	0.8285 MPa	0.9777

With the 3D model, which consists of about 11000 SOLID187 tetrahedral elements each with 10 nodes, a quasi-static analysis was performed. For the nodes of the cylindrical base surface, a fixation was selected as boundary condition. Furthermore, in order to minimize the influence of load application, steel material was assigned to the cylindrical connector on the opposite side of the fluid actuator. This connector was bonded to the fluid actuator. In addition to this, a boundary point R_P and the center point M_Z of the circular surface of this cylinder were generated for practical application of an additional boundary condition and for the evaluation of simulated rotation angle φ_S (see Fig. 2). For this point M_Z, only displacements in the direction z_F were allowed. Furthermore, all nodes of the circular area were selected and the displacement in the direction of z_F were coupled together using the command *cp,1,uz,all*. To sum up, the simulation of the actuator differs from the experimental setup, because in simulation both actuator movements, the rotation and the stroke, are recorded at one and the same actuator side. In the first load step, the load torque M_L was applied on the peripheral surface of the aforementioned cylinder and kept constant through the second load step. Additionally, in the second load step all inside surfaces of the fluid actuator were loaded with a pressure of 1000 mbar.

4.   RESULTS AND DISCUSSION

4.1   Production of a Functional Model

The functional model was produced by injection molding. A special mold of nine parts, without counting screw connections, was manufactured (see Fig. 4a and b). The casting of the inner and outer surfaces of the fluid actuator was realized by five rapid prototyping insertions. In order to improve the releasing procedure of the silicone from the rapid prototyping insertions, which were constructed layer by layer process specific, the insertions were coated with a commercially available clear varnish.
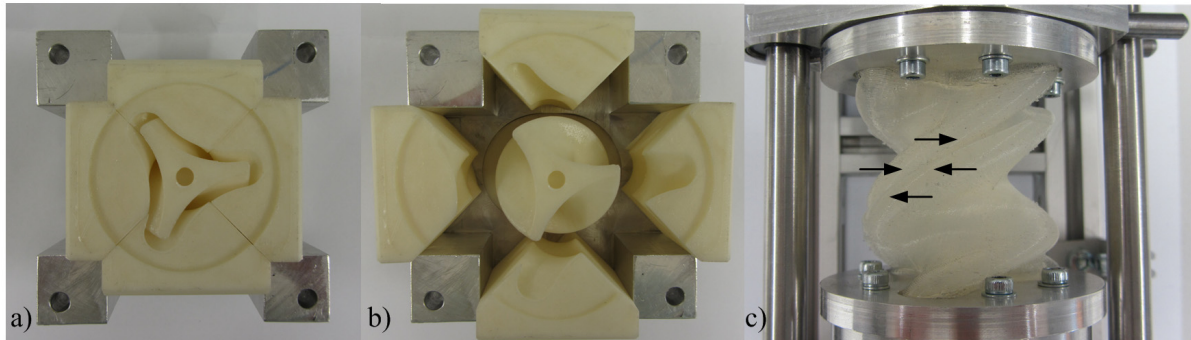

Fig. 4. Lower mold half with five rapid prototyping insertions: a) position of the insertions during the injection molding process; b) position of the insertions after removing the fluid actuator; c) buckling of the functional model at $p = 0$ mbar and $M_L = $ -0.5 Nm

In addition, a cylindrical hole with a diameter of 5 mm in the second cylindrical connector of the fluid-mechanical actuator (deviation to the top view of the actuator without a hole in Fig. 2) is a deviation caused by production. Accordingly, the functional model is open at both ends.

4.2   Measurements on the Functional Model

The functional model was placed in the experimental setup. The cylindrical connectors of the fluid-mechanical actuator were each connected positively with slices over six M3 screws airtight to the mounting plates. Fig. 5 shows pictures taken using a stationary camera (Canon PowerShot SX230, Canon Germany GmbH, Krefeld, Germany) installed on a section of the experimental setup. Thereby, the focus lies on the fluid-mechanical actuator, which is running under increasing internal pressure p and generates a stroke s and a rotation φ with respect to its longitudinal axis. In the range from 0 to about 500 mbar, the fluid-mechanical actuator is operating primarily on the principle of folding (here unfolding) and generates a stroke s and a rotation φ. Above this range, the fluid-mechanical actuator operates mainly on the principle of stretching. As a result, a stroke s is nearly exclusively generated, while the rotation φ takes a back seat (see Fig. 5). The boundary between folding and stretching was determined by a difference quotient.
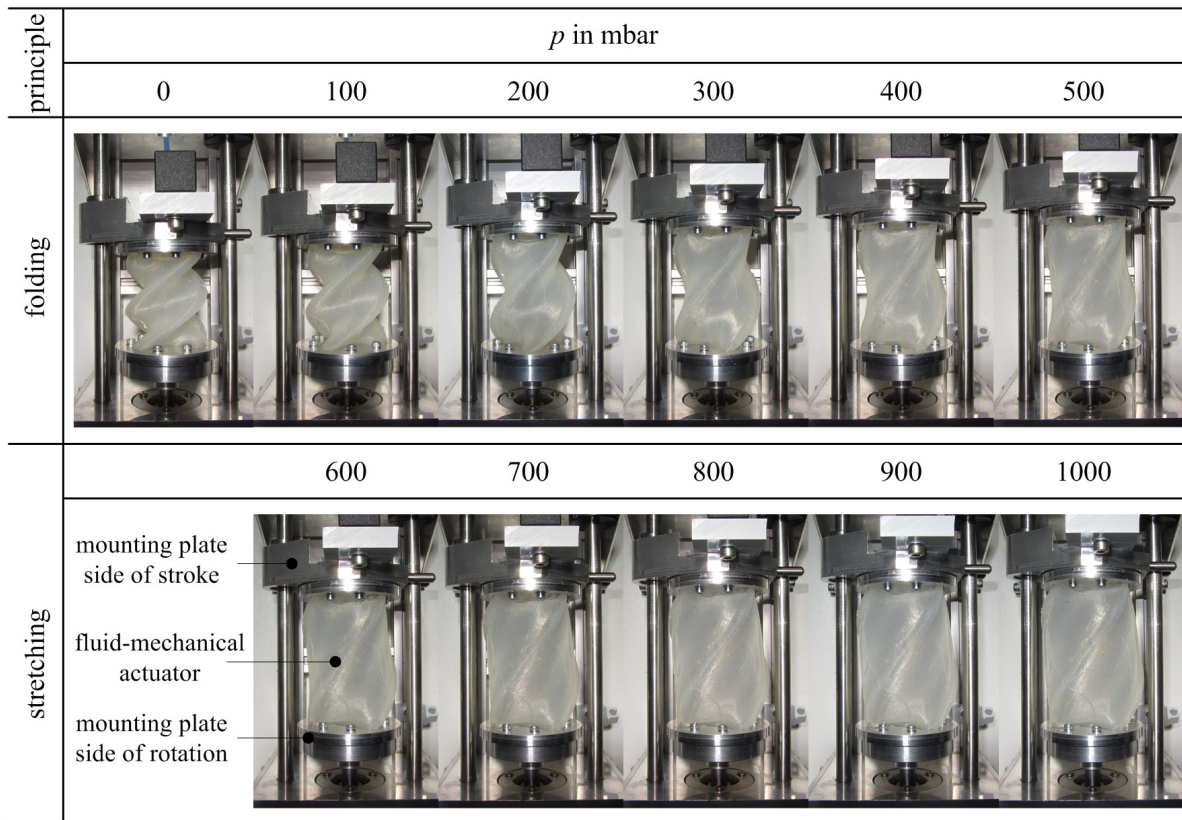
Fig. 5. Section of the experimental setup with a view of the fluid-mechanical actuator under increasing internal pressure p from 0 to 1000 mbar in steps of 100 mbar with classification according to the principle of deformation
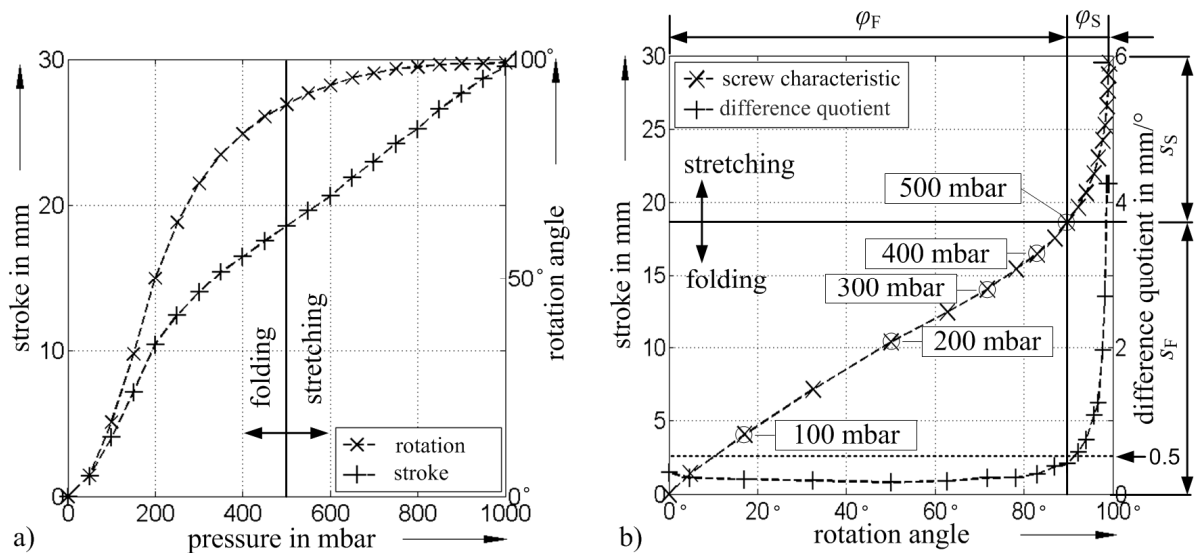

Fig. 6. Characteristics of the function model with $M_L = 0$ Nm under increasing pressure;
a) stroke s and rotation angle φ_M in response to the increasing pressure p;
b) screw characteristic as a function of increasing pressure p and the difference quotient of the screw characteristic curve
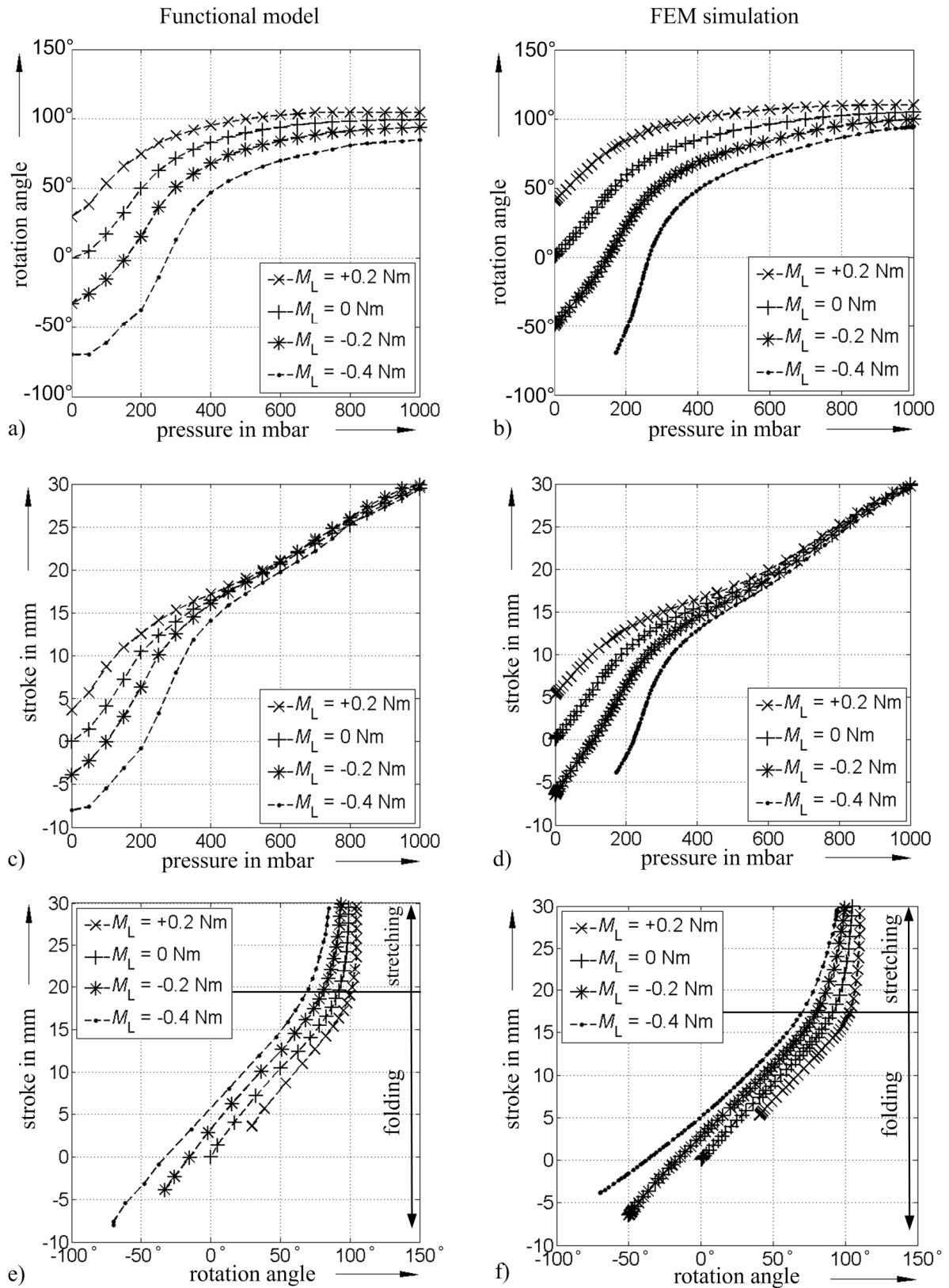
Fig. 7. Measured characteristics of said functional model (a, c and e) and simulated characteristics of the simulation model (b, d and f) at different load torques M_L: a) and b) rotational angle φ_M and φ in response to the increasing pressure p; c) and d) stroke s as a function of increasing pressure p; e) and f) characteristic screw curve in dependence on the rising pressure p

For indication of the actuator deformation principle we propose to use a difference quotient. If the difference quotient composed of the differences between two adjacent measurement points from stroke s divided by the measured angle φ_M is greater than 0.5 mm /°, the functional model operates on the deformation principle of stretching; if it is less, then it is operating on the deformation principle of folding (Fig. 6b, dashed line). Fig. 6a shows the stroke s measured with the laser, and the rotation angle φ_M, measured with the torque measuring shaft by increasing the internal pressure p from 0 to 1000 mbar in steps of 50 mbar with a load torque M_L of 0 Nm (stroke and angle characteristic for $M_L = 0$ Nm). Both curves are increasing monotonically, whereby the rotation angle φ_M for pressures above 500 mbar approaches asymptotically a value of $\varphi_M = 100°$. Both curves exhibit an inflection point in the initial region, which is caused by the friction (see Fig. 9a). If the stroke s is plotted against the rotation angle φ_M for the same pressure values, we obtain the characteristic screw curve of the functional model for $M_L = 0$ Nm (see Fig. 6b). The screw characteristic is approximately linear up to a pressure of $p = 500$ mbar. This is the range in which the actuator predominantly unfolded, and the difference quotient has an average value of about of 0.25 mm / °. From this pressure, the difference quotient of the characteristic screw curve is steadily increasing. The fluid actuator extends almost linearly with increasing pressure p in its axial direction (z_F-direction).

In Fig. 7a, c and e, the measured rotation angle, stroke and screw characteristic curves are mapped under increasing internal pressure p from 0 to 1000 mbar in steps of 50 mbar for the load torque M_L of -0.4 Nm to 0.2 Nm in steps of 0.2 Nm. Here, a negative load torque M_L generates a rising initial torsion angle φ_A and a positive load torque reduces this. If the function model is loaded with a load torques marginally smaller than -0.4 Nm at $p = 0$ mbar, it is due to local instabilities and the functional model is buckling (see Fig. 4c).

All measured rotation angle characteristics (see Fig. 7a) have a monotonically increasing behavior, tending to converge at a saturation value and exhibit an inflection point in the range less than 250 mbar. The measured values for the maximum rotation angle φ_{Mmax} (for this asymptotic approximation) for $p = 1000$ mbar are increasing from 84.75° at $M_L = -0.4$ Nm, via 94° and 99.25° to 104.75° at $M_L = 0.2$ Nm. In addition to this, the measured angle ranges φ_{RM} of the fluid actuator are decreasing from 154.25° at $M_L = -0.4$ Nm, via 127° and 99.25° to 75.25° at $M_L = 0.2$ Nm. This nearly linearly decreasing characteristic is shown in Fig. 8a.
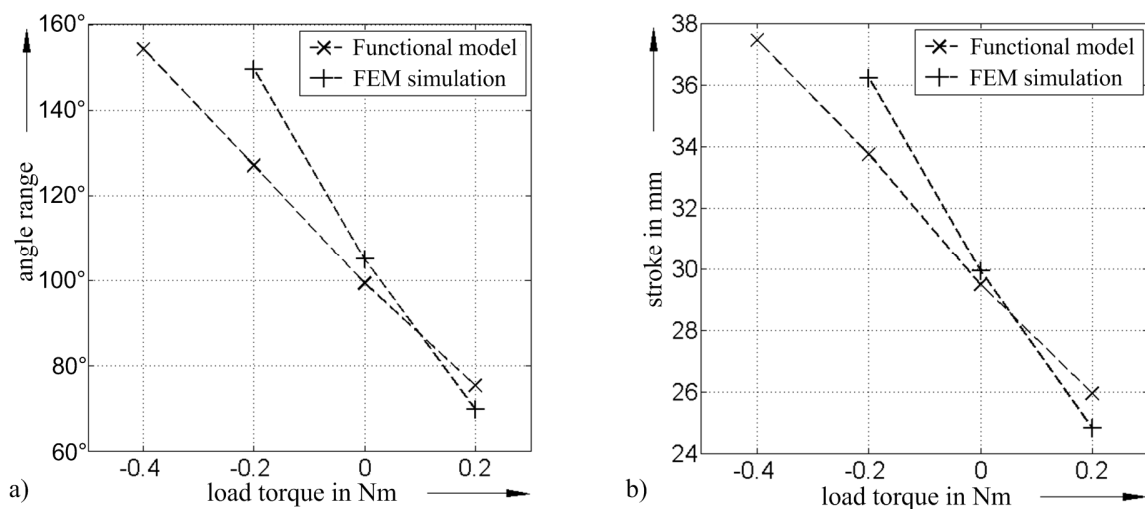

Fig. 8. Simulated and measured a) angle range φ_B and b) stroke range s_B each at $M_L = -0.4$ Nm to 0.2 Nm in steps of 0.2 Nm; (simulation without $M_L = -0.4$ Nm)

The measured characteristic stroke curves (see Fig. 7c) also exhibit a monotonically increasing behavior and an inflection point in the range below 250 mbar. All the characteristic stroke curves approach each other in the range for pressures above 500 mbar. To repeat, this is the stretching operating range of the fluid actuator. In this operating range, the load torque M_L has only a small influence on the family of stroke characteristics. The measured values for the beginning of the stroke s_{Mmin} rise from -8.03 mm at $M_L = -0.4$ Nm, via -3.88 mm and 0 mm to 3.63 mm at $M_L = 0.2$ Nm. The measured stroke range s_{RM} fluid actuator decreases from 37.44 mm at $M_L = -0.4$ Nm, via 33.74 mm and 29.48 mm to 25.93 mm at $M_L = 0.2$ Nm. This nearly linearly decreasing characteristic is shown in Fig. 8b. The measured characteristic screw curves (see Fig. 7e) have a monotonically increasing behavior by increasing internal pressure p. These curves can also be divided into an operating range of folding beneath 500 mbar and into an operating range of stretching above 500 mbar (cp. 6b). In the operating range of folding, the characteristic screw curves are all almost linear. The variables used for this range, which decreases with increasing load torque M_L, are φ_F and s_F (see Tab. 2 and Fig. 6b). In the operating range of stretching of the functional model, a decrease of φ_S and s_S was recorded for increasing load torque $M_L = -0.4$ Nm to 0.2 Nm in steps of 0.2 Nm. However, the change of the stroke by about 1.64 mm is only marginal. This indicates only a small influence of the load torque M_L on the stroke s in this pressure range.

Tab. 2. Functional model and FEM simulation: size of φ_F and s_F for the folding operating range at $0 \leq p \leq 500$ mbar and of φ_S and s_S for the stretching operating range at $500 < p \leq 1000$ mbar for $M_L = -0.4$ Nm to 0.2 Nm in steps of 0.2 Nm

	Functional model				FEM simulation			
M_L in Nm	-0.4	-0.2	0	0.2	-0.4	-0.2	0	0.2
φ_F in °	131	111	89.75	70.25	-	127.29	91.42	63.64
s_F in mm	25.26	21.33	18.60	15.39	-	23.01	17.31	12.72
φ_S in °	23.75	16	9.5	5	31.69	22.28	13.51	5.97
s_S in mm	12.18	11.30	10.88	10.54	13.89	13.21	12.63	12.09

4.3 Simulation of the Compliant Fluid-mechanical Actuator

In Fig. 7b, d and f the simulated rotation angle, stroke and screw characteristic curves are mapped under increasing internal pressure p from 0 to 1000 mbar. Similarly, in the simulation of applying a load torque of -0.4 Nm, the simulation model was buckling (cp. Fig. 4c). This was expressed by convergence problems and a subsequent simulation abort. For this reason, in this simulation it was necessary to use three instead of two load steps. At the first load step, pressure was applied up to 1000 mbar. At the second, the torque was applied up to its maximum. Finally, at the third load step the pressure was lowered again to 0 mbar. The simulation does not converge in the third load step for pressures p less than 172.3 mbar. This corresponds to a simulated rotation angle φ of approximately -69.75° and to a stroke s of approximately -19.7 mm. In this case, this value is close to the experimentally determined value of $\varphi_M = -70°$ for $M_L = -0.4$ Nm, where the buckling is indicated over the nearly horizontal course of the rotation angle characteristic curve (see Fig. 7a). All the simulated rotation angle characteristics (see Fig. 7b) have a monotonically increasing behavior and tend to converge at saturation. The simulated values for the maximum rotation angle φ_{max} (for this asymptotic approximation) at $p = 1000$ mbar are increasing from 94.39° at $M_L = -0.4$ Nm, via 99.64° and 104.92° to 110.10° at $M_L = 0.2$ Nm. In addition to this, the simulated angle ranges φ_{RS} of the fluid actuator are decreasing from 149.58° at $M_L = -0.2$ Nm, via 104.92° to 69.61° at $M_L = 0.2$ Nm. The value of φ_{RS} at $M_L = -0.4$ Nm for the whole pressure range is not available because of the aborted simulation. This nearly linearly decreasing characteristic is

shown in Fig. 8a. The simulated characteristic stroke curves (see Fig. 7d) also exhibit a monotonically increasing behavior and an inflection point in the range between 400 and 600 mbar. All simulated characteristic stroke curves approach each other in the operating range of stretching for pressures above 500 mbar. The simulated values for the beginning of the stroke s_{min} are rising from -6.46 mm at $M_L = $ -0.2 mm via 0 mm to 5.29 mm at $M_L = 0.2$ Nm. The value for s_{min} at $M_L = $ -0.4 Nm was not available because of the aborted simulation. The simulated stroke range s_R of the fluid actuator decreases from 36.22 mm at $M_L = $ -0.2 Nm, via 29.93°mm to 24.81 mm at $M_L = 0.2$ Nm. The value for s_R at $M_L = $ -0.4 Nm was also not available because of the aborted simulation. This nearly linearly decreasing characteristic is shown in Fig. 8b. The simulated characteristic screw curves (see Fig. 7f) have a monotonically increasing behavior by increasing internal pressure p. These curves can also be divided into an operating range of folding beneath 500 mbar and an operating range of stretching above 500 mbar (Fig. 6b). In the operating range of folding, the characteristic screw curves are all almost linear. φ_F and s_F decrease with increasing load torque M_L (see Tab. 2). In the operating range of stretching of the simulated model, a decrease of φ_S and s_S was recorded for increasing load torque $M_L = $ -0.4 Nm to 0.2 Nm in steps of 0.2 Nm. However, the change of the stroke by about 1.80 mm is only marginal and indicates only a small influence of the load torque M_L on the stroke s in this pressure range.

4.4   Consideration of the Friction Torque of the Movable Bearing

If the pressure p is increased at the functional model and a rotation φ and a stroke s is created, the friction in the guideways and bearings is antagonistic to these two motions (see Fig. 2). Thereby, a smaller value for the rotation φ_M and a smaller value for the stroke s are measured theoretically. If the functional model operates without any load, the torque measuring shaft indicates for pressures p greater than zero the friction of the movable bearing (see Fig. 9a). To determine this effect of friction quantitatively on the motion behavior, a comparison of the simulation and measurement of a load case of $M_L = 0$ Nm was analyzed. Therefore, the relative error of the stroke and rotation angle was determined.
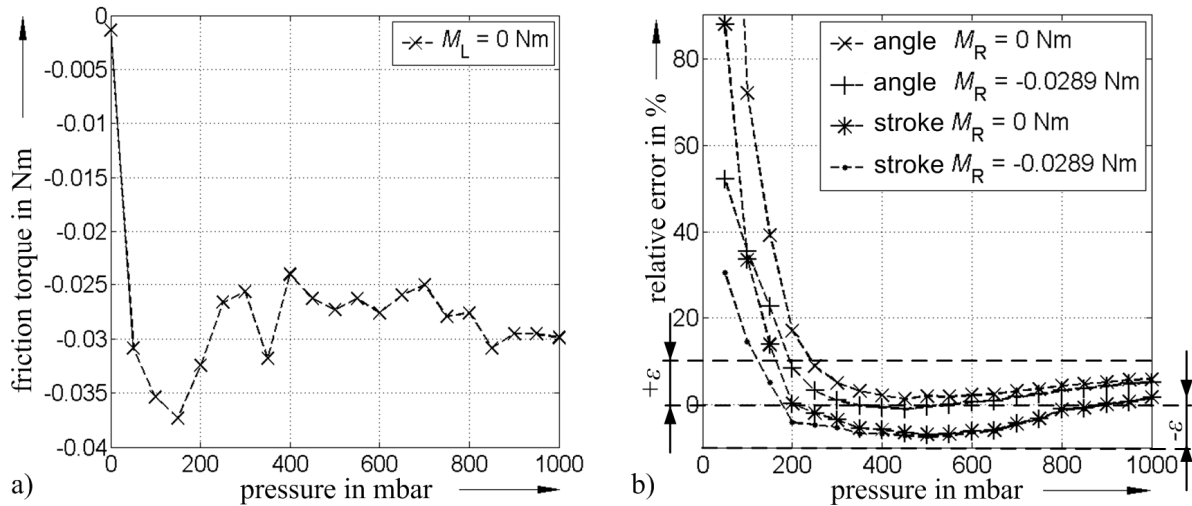

Fig. 9. Friction torque M_R of the movable bearing at load torque $M_L = 0$ Nm: a) friction torque M_R as a function of increasing pressure p and b) relative error of the angle δ_φ and the stroke δ_s as a function of increasing pressure p with and without friction torque M_R

Fig. 9a shows the characteristics of the friction torque M_R with increasing pressure p. Of course, sliding friction is measurable only after overcoming the sticking friction. In other words, the pressure must be above 0 mbar and there must be a motion. For this case, at the

remaining 20 measurement points the average friction was calculated to a value of $M_R = -0.0289$ Nm. Then, a simulation as described in Section 3.3 was performed. Thereby, the friction torque M_R was applied here as a load torque. Next, the relative error of the stroke δ_s and the rotation angle δ_φ was evaluated at $M_L + M_R = 0$ Nm and $M_L + M_R = -0.0289$ Nm with $M_L = 0$ Nm (see Fig. 9b); the value of the relative angular deviation with $\delta_\varphi = 186\%$ at $M_R = 0$ Nm and $p = 50$ mbar is beyond the displayed range. As result, if the friction is considered, the values of the relative angular deviation δ_φ and the values of the relative stroke deviation δ_s are always below the values at which the friction is disregarded. Furthermore, if we calculate the difference of relative angular deviation δ_φ with and without friction and/or the difference of relative stroke deviation δ_s with and without friction for rising pressure values p, we obtain in each case a monotonically decreasing sequence of numbers. This shows the decreasing influence of the friction torque M_R with increasing pressure p (the sequence of numbers is not shown). It should be noted, taking into account the friction, that the relative angular deviation δ_φ decreases over all pressure values and the difference between the simulation and functional model is less. In addition, the relative stroke deviation δ_s decreases for the pressure range 50 mbar $\leq p \leq$ 150 mbar and increases slightly for the pressure range 200 mbar $\leq p \leq$ 1000 mbar. Even more, the relative angular deviation δ_φ and the relative stroke deviation δ_s are in compliance with the friction for pressures of $p \geq 200$ mbar less than 10% ($|\varepsilon| < 10\%$). Neglecting the friction, this low deviation of 10% is jointly achieved for δ_φ and δ_s at $p \geq 250$ mbar. Thus, the validity of the simulation model can be ensured in consideration of the friction over a larger pressure range.

5. CONCLUSION AND OUTLOOK

In conclusion, the selected simulation model of the fluid-mechanical actuator exhibits for the unloaded case a deviation less than 10% for $p \geq 200$ mbar. For this reason, simulation models can be used to support the development of fluid-mechanical actuators for biomedical or other applications. Subsequently, the reproducibility of the presented results must be verified by measurement of a greater number of functional models. Furthermore, factors such as manufacturing variation, measuring inaccuracies and all influences of friction should be investigated and taken into account in future simulation models.

6. ACKNOWLEDGMENTS

REFERENCES

[1] B.A. Taheri, R.T. Knight, and R.L. Smith, "A dry electrode for EEG recording", Electroencephalography and Clinical Neurophysiology, 90, 376-383, 1994.

[2] W.C. Ng, H.L. Seet, K.S. Lee, N. Ning, W.X. Tai, M. Sutedja, J.Y.H. Fuh, and X.P. Li, "Micro-spike EEG electrode and the vacuum-casting technology for mass production", Journal of Materials Processing Technology, 209, 4434–4438, 2009.

[3] A. Searle, and L. Kirkup, "A direct comparison of wet, dry and insulating bioelectric recording electrodes", Physiological Measurement, 21, 271-283, 2000.

[4] P. Fiedler, L.T. Cunha, P. Pedrosa, S. Brodkorb, C. Fonseca, F. Vaz, and J. Haueisen, "Novel TiNx-based biosignal electrodes for electroencephalography", Measurement Science and Technology, 22 (12), ISSN: 09570233, 2011.

[5] S. Griebel, L. Zentner, V. Böhm, and J. Haueisen, "Sensor placement with a telescoping compliant mechanism", IFMBE Proceedings of the 4th European Conference of the International Federation for Medical and Biological Engineering, 22, 1987-1989, Springer, Berlin, 2009.

[6] S. Griebel, V. Böhm, and L. Zentner, "Actuator development based on snail tentacles", Proceedings of the 53rd Internationales Wissenschaftliches Kolloquium der Technischen Universität Ilmenau, ISLE, Ilmenau, 2008.

[7] S. Griebel, S. Klee, P. Bessler, L. Zentner, and J. Haueisen, "Vorrichtung und Verfahren zum adaptiven aktiven Positionieren und Halten von Sensoren auf oder über der Oberfläche eines biologischen Objektes", patent application, DE 10 2010 056 099 A1, 21.06.2012.

[8] S. Griebel, A. Streng, and L. Zentner, "Nachgiebiger Fluidantrieb zur Erzeugung einer nahezu exakten bidirektionalen Schraubenbewegung und dazugehöriges Verfahren", patent specification, DE 10 2011 104 026 B4, 11.04.2013.

[9] P. Meier; M. Lang., and S. Oberthür,"Reiterated tension testing of silicone elastomer", In Plastics, Rubber and composites, UK, Maney Publishing, Vol 43 No 8, 372-377, 2005.

[10] V. Böhm, "Bionisch inspirierte monolithische Gelenkelemente mit fluidmechanischem Antrieb", Verlag ISLE, Ilmenau, 2006.

[11] R. Lichtenheldt, "Konzeption und Aufbau einer Demonstrationsanlage für das Greifen eines Eis", Master thesis, TU Ilmenau, Ilmenau, 2011.

[12] P. Fiedler, S. Griebel, C. Fonseca, F. Vaz, L. Zentner, and J. Haueisen, "Novel Ti/TiN dry electrodes and Ag/AgCl: A direct comparison in multichannel EEG", European IFMBE MBEC 2011, Budapest, Hungary, 2011.

[13] S. Griebel, P. Fiedler, A. Streng, J. Haueisen, and L. Zentner, "Erzeugung von Schraubenbewegungen mittels nachgiebiger Aktuatoren", Berichte der Ilmenauer Mechanismentechnik 1 - Mechanismentechnik in Ilmenau, Budapest und Niš, Ilmenau, Universitätsverlag Ilmenau, Ilmenau, 91-102, 2012.

[14] A. Streng, "Entwicklung und Untersuchung einer nachgiebigen Struktur zur Erzeugung einer rotatorischen Bewegung", Diploma thesis, TU Ilmenau, Ilmenau, 2008

CONTACTS

Dipl.-Ing. Stefan Griebel   stefan.griebel@tu-ilmenau.de
Dipl.-Ing. Martin Feierabend   martin.feierabend@tu-ilmenau.de
Dipl.-Ing. Attila Bojtos   bojtos@mogi.bme.hu
Prof. Dr.-Ing. habil. Lena Zentner   lena.zentner@tu-ilmenau.de